Estimation of Forest Canopy Height Over Mountainous Areas Using Satellite Lidar

Zhou Fang and Chunxiang Cao

***Abstract*—The full waveform data of the large-footprint Geoscience Laser Altimeter System (GLAS) on the Ice, Cloud, and land Elevation Satellite, together with airborne light detection and ranging (lidar) data, were employed to retrieve the basal-area weighted mean height (Lorey's height) over sloping terrain in the Qilian mountains region, western China. Over mountainous areas with high relief and complex terrain, a GLAS waveform is characterized by multiple energy peaks, which ground and surface objects may be broadened and mixed, making the extraction of canopy height difficult. This study focuses on forests in a mountainous area to derive mean tree height directly from the GLAS waveform information and Gaussian decomposition results. We derived a relationship between the weighted mean tree height derived from airborne lidar data and the predicted mean tree height within the GLAS footprints; the resulting equation explained 82.8% of variance, with an RMSE of 2.8 m. Based on the analysis of different slope categories, it can be demonstrated that the proportion of energy and characteristics of the Gaussian curves greatly influenced the extraction of mean tree height in mountainous areas.**

***Index Terms*—Gaussian decomposition, Geoscience Laser Altimeter System (GLAS), Ice, Cloud, and land Elevation Satellite (ICESat), light detection and ranging (lidar), mean tree height, mountainous areas.**

I. Introduction

TREE height is the basis for dividing forest layers and one of the leading dimensions of ecological variations among tree species. Not only does it reflect the forest land productivity, it is closely related to the standing volume and volume growth rate [1]. In recent years, with the rapid development of lidar remote sensing, national or regional forest resources inventory faces an opportunity, also a challenge. Lidar remote sensing is divided into three platforms—ground, airborne, and spaceborne according to platform height [2]. According to different recording modes of return signals, it can be divided into full waveform lidar data and discrete-return lidar data. The former is mainly used for assessing forest vertical structure parameters at large scales, from regional to continental and global extents, the latter provides the best measurement accuracy of terrain elevation and vegetation height, even on sloped terrain or for dense forests.

Manuscript received July 26, 2013; revised November 17, 2013; accepted January 06, 2014. Date of publication January 27, 2014; date of current version August 21, 2014. This work was supported in part by the Natural Science Foundation of China (Grant 41171330) and in part by National High Technology Research and Development Program of China (Grant 2013AA12A302).

The authors are with the State Key Laboratory of Remote Sensing Sciences, Institute of Remote Sensing and Digital Earth, University of Chinese Academy of Sciences, Chinese Academy of Sciences, 100101 Beijing, China (e-mail: fangzhou@irsa.ac.cn; cao413@irsa.ac.cn).

Color versions of one or more of the figures in this paper are available online at http://ieeexplore.ieee.org.

Digital Object Identifier 10.1109/JSTARS.2014.2300145

Lidar is one of the most promising technologies in forestry, which shows potential for timely and accurate measurement of forest biophysical properties over time [3], [4]. Whether using the high density point cloud data to assess individual tree parameters [5]–[7], low density point cloud data are used to derive measurements at stand scale [8]–[10], or the large footprint, full waveform data satellite lidar data for regional and even global scale forest inventories [11]–[15] are actively promoting the overall level of lidar researches in forestry application. However, in the face of massive data and pricey fares, airborne lidar data are usually limited to local or regional scale, rarely at the extent of country-level or continental-level. But point cloud data can be used as calibration data for large footprint data in regional forest resources inventory.

Large footprint, full waveform satellite lidar data, such as data provided by the Geoscience Laser Altimeter System (GLAS) aboard the Ice, Cloud, and land Elevation Satellite (ICESat), record a continuous stream of data from the returned lidar pulses, as these reflect the vertical distribution of the terrain and vegetation within each footprint. Original waveform analysis includes direct measurement [16] and waveform decomposition. GLAS waveforms can be considered as the sum of individual Gaussian returns reflected from each element within the footprint [17], [18]. Modeling forest characteristics from GLAS waveform metrics is another approach. Lefsky *et al.* [19] used three waveform metrics to estimate mean tree height, and estimated forest canopy height with an *RMSE* of 5 m (83% of variance in forest canopy height explained). Popescu *et al.* [20] compared forest parameters derived from GLAS and airborne lidar, results indicated a very strong correlation for terrain elevations between GLAS and airborne lidar. Sun *et al.* [21] found that a high correlation existed between airborne lidar measures of canopy height and GLAS measures of canopy height, based on quartile energies from both data. GLAS waveforms from flat, homogenous terrain can be directly and quickly extracted [21]. Over mountainous areas with large relief and complex terrain, the peaks from ground and surface objects can be broadened and mixed, making the identification of ground elevation and tree structural parameters difficult [22]. China is a mountainous country, having two-thirds of the area occupied by mountains. We should make good use of GLAS waveforms in the mountains, they can provide so much information, and account for a very large proportion. Researchers focused on the use of GLAS data to extract maximum tree height over mountainous areas [23]–[25], but few studies focused on mean tree height. Gaussian decomposition is an excellent and well-documented method to derive height information from GLAS waveform. And many metrics directly extracted from GLAS waveform should be

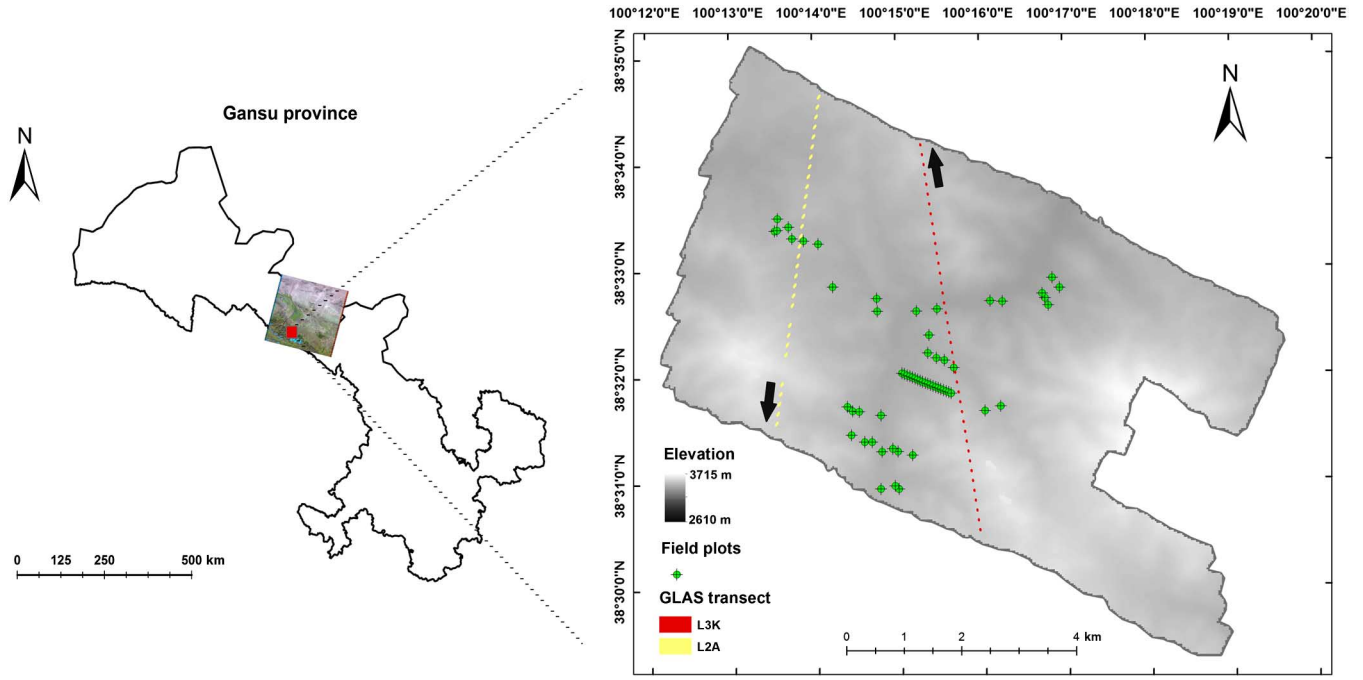

Fig. 1. (Left) Gansu province administrative zoning map, the image on the right side Gansu layout is one TM image, the red area represents the location of our study area. (Right) GLAS footprints over our study area, only the GLAS shots acquired under no or low cloud conditions were chosen, which include L2A (down arrow) and L3K (up arrow).

researched in mean tree height extraction. Maximum height is subjected to large sampling error in the field, in contrast to mean tree height which is the average of a number of observations [19]. Meanwhile, recent studies show that small footprint airborne lidar is useful for estimating forest stand variables that include mean tree height even with low point cloud density [26]–[29].

In this study, airborne lidar data were used to derive regional mean tree height, and field surveying data were used to validate the airborne data. A classification map derived from TM image was used to select the GLAS footprints which were in vegetation covered areas. The main objectives of this study are to 1) develop an accurate Gaussian decomposition to consistently account for the influence of terrain in moderate and high relief areas, 2) utilize mean tree height derived from airborne lidar data and GLAS waveform metrics to explore what metrics influence the mean tree height over mountainous areas, and 3) examine how terrain slopes affect the utility of GLAS waveform metrics to model mean tree height.

II. Study Area and Data

A. Study Area

Our study site of Dayekou is situated in Qilian Mountains. Qilian Mountains cover three plateaus, including Qinghai-Tibet, Inner Mongolia-Xinjiang, and Loess, western China. According to the SRTM data with a resolution of 1-arc second, the elevation varies from 2500 to 3800 m above the sea level. The landscape is composed of high mountains and deep valleys, a mean slope of 9.95°, with a maximum of 56.26°. Temperature fluctuation is large, rainfall focuses on summer, temperature and precipitation change significantly as altitude increases.

Evergreen coniferous natural secondary forest is the main forest vegetation type in the study area. The *Picea crassifolia* and *Sabina przewalskii* are major tree species which widely distribute in the eastern Qilian, the former constitutes the main forest part and the latter forms a sparse stand in the alpine and subalpine sunny slope zones. Fig. 1 shows the location of the area and the selected GLAS data.

B. Field Measurements

Filed measurements were acquired to provide accuracy information for measurements, such as diameter at breast height (DBH), tree height, and crown breadth. Filed data were acquired during June 1–28, 2008 at 63 square-shape plots. Each sample plot's size was $25\ \mathrm{m} \times 25\ \mathrm{m}$. Caliper, laser range finder, LAI-2000, surveyor's pole, and tape measure were used to measure DBH, tree canopy height, LAI, height under branch, and crown breadth in two main directions, respectively (Table I). The heights were measured for all the sample trees (DBH greater than 2.5 cm), and for each plot the mean height was computed as the Lorey's height which weights the contribution of trees to the stand height by their basal area [30]. Lorey's height (h_L) was calculated by multiplying the tree height (h) by its basal area (g), and then dividing the sum of this calculation by the total stand basal area:

$$h_L = \frac{\sum g * h}{\sum g}. \tag{1}$$

C. Airborne Lidar Data

Airborne lidar data were acquired in June, 2008 from an average altitude of 760 m above ground level. The lidar system (IGI-Litemapper 5600) with laser scanner Riegl LMS-Q560 used

TABLE I
SUMMARY STATISTICS OF 63 FIELD SAMPLE PLOTS (25 m × 25 m) IN QILIAN MOUNTAINS

Symbol	Mean	Minimum	Maximum
Density (number of trees)	37.00	12.00	150.00
Diameter (cm; 1.3 m aboveground)	16.31	3.07	47.10
Mean height (m)	10.07	4.26	15.01
Lorey's height (m)	13.90	4.79	19.83
Maximum height (m)	18.75	6.44	26.52
Mean crown length (m)	4.33	1.16	8.74
Leaf area index (LAI) (m^2/m^2)	2.92	1.41	5.76
Biomass (t/ha)	114.46	36.88	174.83

a narrow scan angle of <0.5 mrad either side of NADIR and with a point density of about $1\ \mathrm{return/m^2}$. The reported horizontal and vertical accuracies with the Litemapper 5600 system are 10 and 3 cm, respectively, the average footprint size was 38 cm. The x, y, and z positions (easting, northing, and elevation) and intensity of each pulse were supplied for the first and last pulse and geo-referenced to WGS 1984, UTM Zone 47 N.

D. ICESat/GLAS Data

The NSIDC (National Snow and Ice Data Center) disseminates 15 Level-1 and Level-2 GLAS data products (http://nsidc.org/data/icesat/). The ICESat's science mission launched on January 12, 2003, after 7 years in orbit and 18 laser-operations campaigns, it ended due to the failure of its primary instrument. ICESat was equipped with three lasers, all three of the ICESat lasers stopped collecting data, L1 on March 29, 2003, L2 on October 11, 2009, and L3 on October 19, 2008. The products used in this study included GLA01 (L1A Global Altimetry) and GLA14 (L2 Land Surface Altimetry) from Release-33. GLA01 contains transmitted and received waveforms from the altimeter, and GLA14 contains surface elevations for land and the laser footprint geolocation and reflectance.

GLAS waveforms might be contaminated by the atmospheric forward scattering or saturated signals, only the cloud-free (the flag $FRir\_qaFlag = 15$ in the GLA14 products) and saturation-free (the saturation index $satNdx = 0$ in the GLA14 products) shots were selected [22]. The footprints including the subcycles of L2A (September–November 2003) and L3K (October 2008) were analyzed in this study.

E. Multispectral Optical Imagery

A Landsat-5 TM scene from September of 2009 was obtained from USGS EROS Center. The scene consists of six spectral bands with a nominal spatial resolution of 30 m were used. Radiometric and ortho-rectification were applied to the image.

III. METHODS

A. Airborne Lidar Data Processing

Terrascan (Terrasolid, http://www.terrasolid.fi/en) possesses several useful options for point cloud classification. Before classifying point cloud data, we should first filter out exceptional pulses identified as below the nominal ground surface or above the expected canopy height via visualizations. Both digital surface model (DSM) and digital elevation model (DEM) have been obtained from the classification, which was herein performed using a strategy based on a set of "filtrations of the filtrate" [31]. The workflow can be summarized as follows: 1) low point classification, 2) isolated points classification, 3) air points, 4) ground classification, 5) classification of points below surface, 6) classification of points by class, and 7) classification of points by height from ground for different heights.

We defined a "ground" surface by applying the progressive triangulation irregular network (TIN) densification method by Axelsson [32]. The algorithm starts from a coarse TIN surface obtained from reference points which are neighborhood minima. Then new points are added, in an iterative way, if they meet criteria based on distances to TIN facets and angles to the vertices of the triangle. First, selected points with the highest confidence of lying on the ground are selected, and then the program adds to the model other points which fulfill specified criteria. One of these criteria is the maximum size of buildings, describing area of search windows in which at least one point must be a ground point. Iteration distance represents maximum altitude difference in building triangle, and iteration angle characterizes angle between an added point and vertex of the closest triangle. In this study, parameters were applied: max building size 30 m, terrain angle 88°, iteration angle 9°, iteration distance 2 m, and reduce iteration angle when edge length <5 m. The DEM was created using TerraModeller on the basis of the classification of terrain and offterrain objects performed using the whole processing chain from steps 1) to 7). Nonground points were interpolated into a DSM with the same method. The raster DEM and DSM of 1 m spatial resolution were generated.

Normalized digital surface model (nDSM) represented the absolute elevation of earth surface features, for preparing of nDSM, the DEM should be subtracted from DSM. Considering the distribution of tree height, the nDSM values less than 1.5 m and greater than 35 m were removed. For each sample plot, several commonly used and newly proposed metrics [33]–[36] were derived from the vegetation points including 25th percentile (h_{25}), 50th percentile (h_{50}), 75th percentile (h_{75}), 95th percentile (h_{95}), maximum value (h_{max}), mean value (h_{mean}), minimum value (h_{min}), coefficient of variation, skewness, standard deviation, kurtosis, and canopy cover percentiles.

B. GLAS Data Processing

The appropriate GLAS footprints should be selected before processing. GLAS footprints overlaid on the TM-generated classification map can identify the categories to which the foot-prints belong. Fig. 2 introduces the flowchart of TM image classification. The maximum likelihood classifier was applied to the image spectral information, texture information, normalized difference vegetation index (NDVI) and other auxiliary geographic data to differentiate trees, shrubs, and grassland. We had the field investigation data of the whole area to train samples and evaluate the classification precision. The classification produced

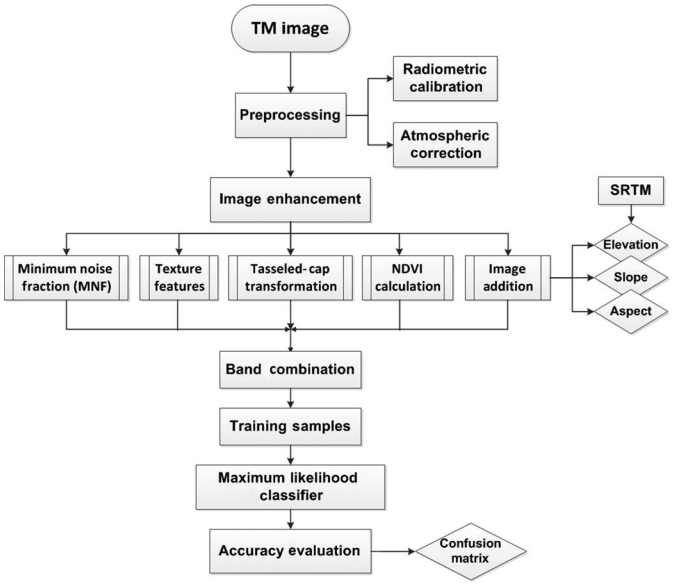

Fig. 2. Flowchart of TM image classification.

an overall accuracy of 90.4%. Finally, we selected 66 GLAS footprints which were in vegetation covered areas.

The raw GLAS waveform data can be converted from record counts to volts using a conversion table [37] and normalized by the total received energy. The purpose of the normalization was to enable comparison of waveforms captured in different epochs. A GLA01 waveform was linked to a GLA14 location by index and shot number. In order to keep the georeference systems consistent, the coordinates of GLAS waveforms were converted from the TOPEX/Poseidon ellipsoid to the WGS-84 ellipsoid. GLAS data record the laser energy returned from an ellipsoidal footprint. The size and ellipticity of a footprint varied through the course of the mission. The major axis radius, azimuth angle, and eccentricity in the GLA14 product (*D_Tpmajoraxis*, *D_Tpazimuth*, and *D_Tpeccentricity*) were used to extract the exact shape of the GLAS footprint based on elliptic parameters equation. The voltage waveform was smoothed by a Gaussian filter of a width similar to the transmitted laser pulse to eliminate some system noise effects [21]. The convolution of the filter and the raw waveform can reduce high-frequency noise and improve the signal-to-noise ratio (SNR). The smoothed waveform was filtered above a threshold which was a function of the mean and standard deviations of background noise (GLA01 product variables *D_4nsbgmean* and *D_4nsbgsdev*). The threshold was set to the mean background noise plus 3.2 times the standard deviation [38].

To explain the complex peaks, Gaussian decomposition was used to decompose each waveform into multiple Gaussian distributions, and then a waveform can be defined by the sum of a series of Gaussian curves [39]:

$$w(t) = \varepsilon + \sum_{m=1}^{N_p} A_m e^{\frac{-(t-t_m)^2}{2\sigma_m^2}} \tag{2}$$

where $w(t)$ is a single-valued curve with parameters $\{\varepsilon, A_m, t_m, \sigma_m\}$ for $m = 1, \ldots, N_p, m$ is the number of Gaussian peaks found. The noise offset estimation, amplitude, position, and half-width of each Gaussian are denoted by ε, A_m, t_m, and σ_m, respectively.

First, the number of Gaussian components within the waveform was estimated from the number of inflection points in the smoothed waveform. A single Gaussian has two inflection points and that when n Gaussians are combined there will be $2n$ inflection points. By solving the first-order and second-order partial derivatives of $w(t)$ and letting them be zero, the initial position and half-width estimates for each component Gaussian can be derived from the locations and separations of consecutive inflection points. Initial amplitude parameters for all component Gaussians were estimated using the Levenburg–Marquardt Least Squares technique which minimized the weighted sum of squares between the observed waveform and its Gaussian decomposition [40].

Inflection points caused by noise should be removed, so that amplitudes were constrained between zero and the maximum return, half widths were greater than 0.1 m, curve peaks were greater than 1 m apart [41]. The position, half-width, and amplitude of each Gaussian curve were determined by the adjacent odd and even inflection points [37]. Two adjacent Gaussian curves, if their interval was less than the transmit pulse width, the smaller Gaussian curve was merged to the larger Gaussian curve. Then, these Gaussian curves were sorted by area sizes. The Gaussian curve was removed if its area was less than 5% of others. Otherwise, the Gaussian curves were merged either by weighting them by area, or by averaging them. The number of Gaussian components was constrained that less than or equal to six. We thus write [37]:

$$\begin{cases} Area_{new} = Area_1 + Area_2 & \\ A_{new} = Max(A_1, A_2) & a = Area_1/Area_2 \\ \sigma_{new} = a * \sigma_1 + b * \sigma_2 & b = 1 - a \\ t_{new} = a * t_1 + b * t_2 & \end{cases} \tag{3}$$

where a and b are area weights, A_{new}, σ_{new}, and t_{new} are the amplitude, half-width, and position of the merged Gaussian curve, respectively.

To compare elevation derived from airborne lidar and GLAS data at the footprint level, the airborne lidar nDSM pixels that fell within a GLAS footprint were averaged to product an overall elevation based on their distance to the GLAS centroid following equation [18], [20], [22]:

$$\begin{cases} w = \exp\left\{-2 \cdot \left[(x'/a)^2 + (y'/b)^2\right]^{1/2}\right\} \\ x' = (x - x_0)\sin\alpha + (y - y_0)\cos\alpha \\ y' = (y - y_0)\sin\alpha - (x - x_0)\cos\alpha \end{cases} \tag{4}$$

where w is the weight for any airborne lidar nDSM pixels within a footprint; a and b are semi-major and semi-minor axes of the footprint ellipse; α is the orientation of the major axis that is defined clockwise with respect to the north direction; (x, y) and (x_0, y_0) are the coordinates for the pixel and the footprint center.

Fig. 3 shows a typical GLAS waveform from our study area with the Gaussian peaks from the aforementioned Gaussian decomposition. For the land surfaces, the waveform has 544

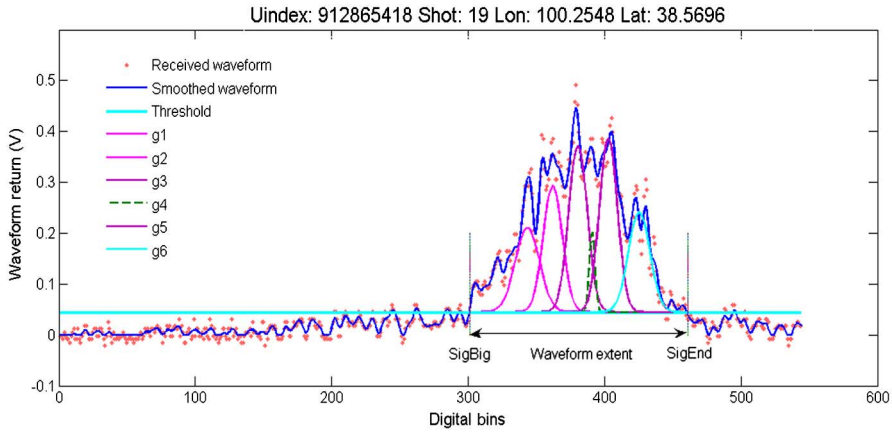

Fig. 3. Typical GLAS waveform in the study area: dots—GLAS waveform data from GLA01, blue solid curve—the waveform after smoothing by a Gaussian filter and other solid curves—Gaussian peaks used to fit the waveform from Gaussian decomposition and threshold value.

TABLE II
DESCRIPTIONS OF GLAS WAVEFORM METRICS

Metric	Description
h_w	The weighted height of airborne lidar nDSM pixels within a GLAS footprint
wf_extent	The distance between *SigBig* and *SigEnd*
wf_max_e	The maximum energy value in the waveform
startpeak	The distance between the beginning of the signal and the position of *wf_max_e* (Duncanson *et al.* [41])
peakend	The distance between the end of the signal and the position of *wf_max_e* (Duncanson *et al.* [41])
f, e_{vs}	Front slope and vegetation to surface energy ratio from waveform (Sun *et al.* [21], Nelson *et al.* [43])
wf_variance	The variance of the waveform
wf_skew	The skew of the waveform
$h_{25}, h_{50}, h_{75}, h_{100}$	Heights of energy quartiles from signal start to signal end, measured from the ground peak (Sun *et al.* [21])
e_14,e_24,e_34,e_44	The proportion of energy in four equal elevation divisions (Duncanson *et al.* [41])
E_14,E_24,E_34,E_44	The proportion of energy in four equal energy return divisions (Duncanson *et al.* [41])
n	Number Gaussian peaks determined by Gaussian decomposition ($1 \le n \le 6$)
l_{gn}	Location of Gaussian peaks determined by Gaussian decomposition
a_{gn}	Amplitude of Gaussian peaks determined by Gaussian decomposition
w_{gn}	Width of Gaussian peaks determined by Gaussian decomposition
r_{gn}	Area of Gaussian peaks determined by Gaussian decomposition

bins with a bin size of 1 ns or 15 cm. The bin size from bin 1 to 151 has been changed to 60 cm starting from acquisition L3A [21]. The noise mean and standard deviation were extracted from GLA01 data to set the threshold which was used to locate the signal beginning (*SigBig*) and end (*SigEnd*). Above the threshold, the smoothed waveform can be decomposed into n components. Over mountainous areas, as with dense canopies, the location of the ground peak becomes formidable. Some metrics were directly derived from the smoothed GLAS waveform and corresponding Gaussian curves for utility to estimate mean tree height (Table II).

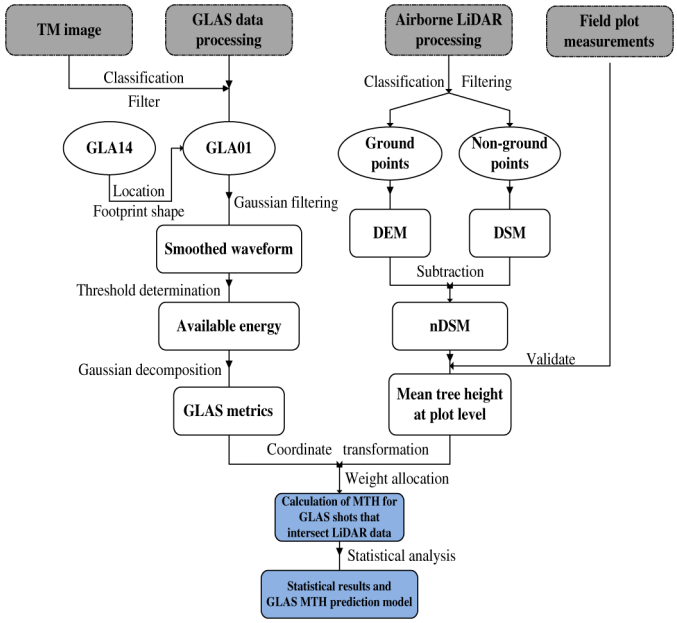

Fig. 4. Conceptual overview of the methodology used in this study.

C. Conceptual Overview

Fig. 4 gives a conceptual overview of the methodology described above.

IV. RESULTS AND DISCUSSION

A. Height Derivation With Airborne Lidar

As were mentioned previously, the metrics can be calculated from a cumulative histogram of lidar nDSM in each plot.

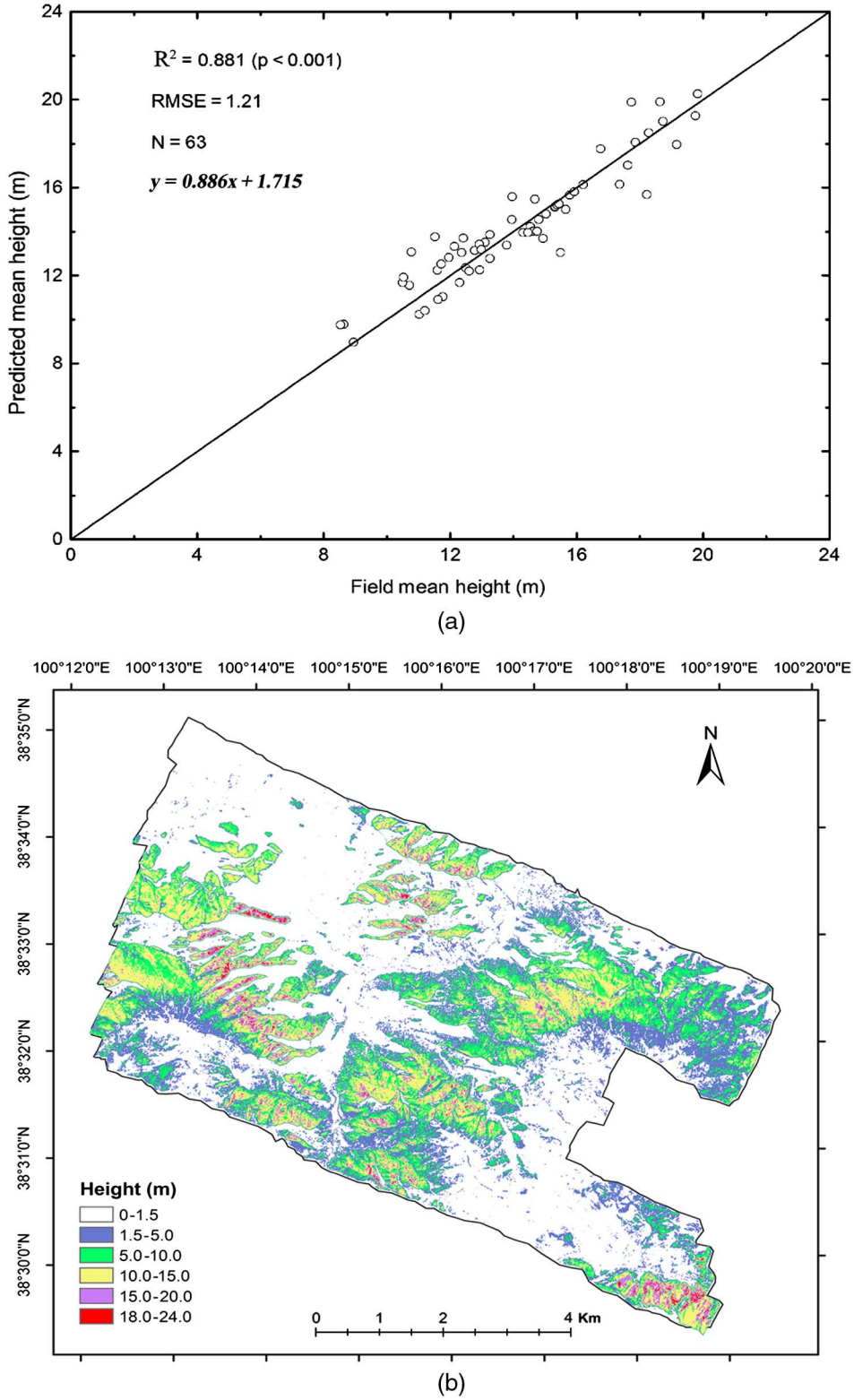

Fig. 5. (a) Observed (x) versus predicted mean tree height (y) by the regression model, using h_{95} and h_{25}. The solid line is a 1:1 line. (b) Image of mean tree height predicted from lidar data over the study area using (5).

Based on field surveying data, linear regression models were built from the sample plots. To examine collinearity, the variance inflation factor (VIF) testing can detect whether or not collinearity exists (no significant collinearity exists if VIF is below 10). The VIF is the reciprocal of tolerance: $1/(1-R_i^2)$, where R_i^2 represents the proportion of variance in the ith independent variable that is associated with the other independent variables in the model [43]. The model identified via regression analysis for estimating plot-level mean tree height took the following form:

$$h_L = 1.959 + 0.627 * h_{95} + 0.401 * h_{25}. \quad (5)$$

This model for plot-level field-based Lorey's mean height (h_L) comprised the quantiles corresponding to plot-level 25th percentile (h_{25}) and 95th percentile (h_{95}) heights, resulting in adjusted coefficient of determination (R^2) of 0.881. The results showed that the regression model was reliable and stable, and all of the variables were statistically significant ($F = 149.77$, $p < 0.001$). The VIF values of the two independent variables were less than 10 and it can be concluded that no significant collinearity exists between the variables.

The scatter plots in Fig. 5(a) show the field-based versus predicted lidar-based plot-level measures of Lorey's mean height. The standard error of the regression (*RMSE*) for the model was 1.21 m.

Since the regression model established a functional relationship between the Lorey's mean height and the lidar data, we can obtain a map of Lorey's mean height distributions over the entire extent of the lidar data coverage. In accordance with the sample plot size, mean height map derived with lidar data provided at a $25\ \mathrm{m} \times 25\ \mathrm{m}$ grid cell resolution [Fig. 5(b)].

B. Gaussian Decomposition

Under flat topographic condition, the result of Gaussian decomposition is shown in Fig. 6(a). Not only obvious Gaussian curves, but nonobvious Gaussian curves that met the standards can be obtained by Gaussian decomposition. The peaks from ground and trees can be broadened and mixed over steep mountainous areas, causing some errors within Gaussian curves. But the overall fit results can be accepted [Fig. 6(b)]. The residuals, calculated as the difference between the original smoothed waveform and the best-fit profile, are shown in the lower panel of Fig. 6.

The position, half-width, and amplitude of each Gaussian curve generally represent the position, slope, and roughness of each reflective surface. Through Gaussian decomposition, not only does it improve the precision of ranging, it can accurately locate the height of each reflective surface within a footprint. We constrained the number of Gaussian curves between 1 and 6 for a more simplistic and comparable approximation of GLAS waveforms because of complicated calculation. More or less the steep slope terrain would make predicting terrain relief difficult. The GLAS footprint diameters were closer to about 100 and 60 m for L2A and L3K in the area. The fit errors were relative small in flat regions. As slopes rise, the fit errors became greater. On the other hand, the impact of footprint size from L2A may be more obvious than these from L3K. It was interesting to observe that, whereas in steep regions, the fit errors may be small because of low vegetation coverage and height.

C. Mean Tree Height Models With GLAS Metrics Inputs

In the process of data modeling, data preprocessing such as the normalization of the data is very important when dealing with GLAS metrics of different units and scales. Normalization can scale all numeric variables in the range [0, 1]. Stepwise multiple regression was used to find a relationship between weighted lidar height and GLAS waveform metrics. Two slope categories were

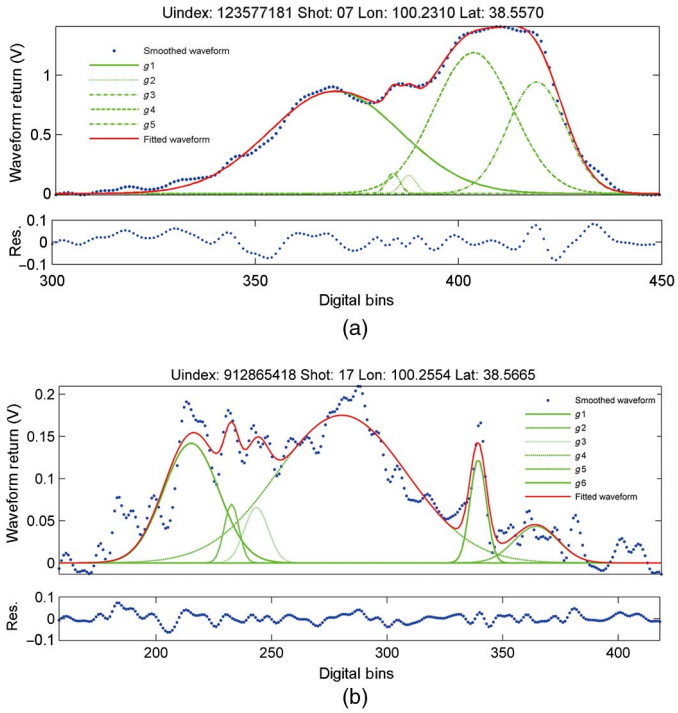

Fig. 6. Gaussian curves between *SigBig* and *SigEnd* from Gaussian decomposition and residuals of the fit in (a) flat and (b) steep regions.

defined as 0°–20° and >20° represented moderate and steep regions, respectively. A leave-one-out cross-validation method (LOO-CV) [44], [45] was used to estimate any quantitative measure of fit that is appropriate for the data and model, through a comparison of the root-mean-squared-error for cross-validation ($RMSE_{cv}$) and *RMSE*. The mean tree height models for each category with associated sample numbers, adjusted R^2, *RMSE*, and $RMSE_{cv}$ are listed in Table III. All of the variables were statistically significant ($p < 0.001$) except the constant of the model for the >20° slope category ($p < 0.05$). After the models were calibrated and validated, de-normalization should be carried out. The model for the 0°–20° slope category had an adjusted R^2 of 0.870 and required five input GLAS metrics. The height model for the >20° slope category had an adjusted R^2 of 0.767, and four input GLAS metrics. Although it does not perform well under steeper condition (>20°), this model indicates that it is possible to directly derive mean tree height from GLAS waveforms even from areas of high relief.

Fig. 7(a)–(c) shows the results of the predicted mean tree height within the GLAS footprints against the weighted height derived from lidar data for the terrain slope categories of 0°–20°, >20°, and all data, respectively. One outlier found in the model for all data pertained to footprint 27. We found that the forest vegetation was only located toward the edge of the footprint by overlapping footprint with the lidar-derived tree height map. This can be easily understood by the energy distribution within a GLAS footprint. The standardized residual plot of the model for all data [Fig. 7(d)] shows that all points are within $[-2, 2]$, which indicates that the model satisfies normality (and homogeneity of variance). The collinearities of the three models were examined by detecting VIF values of the independent variables and the

TABLE III
CALIBRATION RESULTS OF LOREY'S MEAN HEIGHT MODELS, CONSIDERING DIFFERENT SLOPE CATEGORIES

Slope category (°)	n	Model	Adjusted R^2	$RMSE$ (m)	$RMSE_{cv}$ (m)
All	66	$h_w = 0.152 + 0.608*wf\_extent + 0.573*E\_14 - 0.362*e\_14 - 0.239*e\_44 + 0.287a_{g4}$	0.828	2.81	3.47
0–20	31	$h_{w1} = -0.128 + 0.754*startpeak + 0.841*E\_14 + 0.292*E\_44 - 0.730*e\_44 + 0.315*w_{g4}$	0.870	2.22	2.47
>20	35	$h_{w2} = 0.593 - 0.418*e\_14 - 0.453*e\_44 + 0.786*a_{g4} + 0.153*w_{g6}$	0.767	3.10	3.53

66 GLAS footprints meet requirements with one outlier removed.

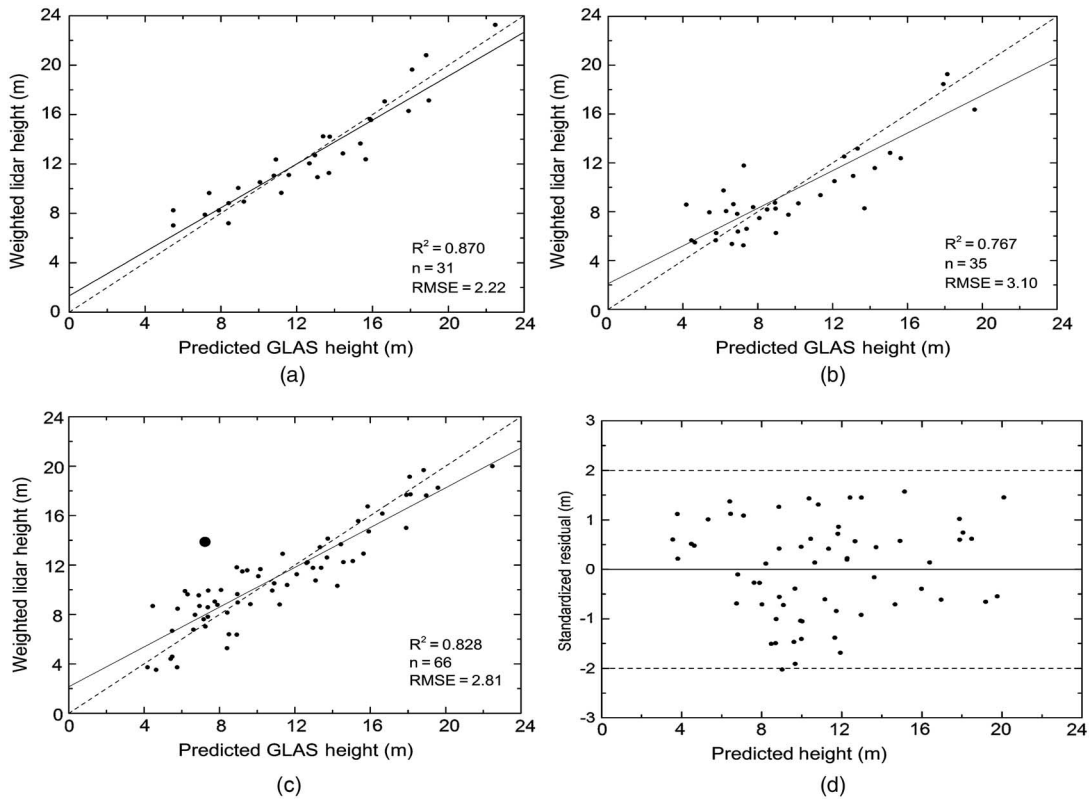

Fig. 7. Scatter plots of the weighted mean tree height (m) derived from lidar data against the predicted mean tree height (m) within the GLAS footprints for slope categories of (a) 0°–20°, (b) >20°, (c) all, and (d) plot of standardized residual against predicted mean tree height after removing the outlier in all data slope category. The dash line is a 1:1 line and the solid line is the best-fit line.

results showed that no significant collinearity existed between these variables.

In the 0°–20° slope category, *startpeak* increases consistently with mean tree height. *E_14*, the proportion of energy in the lowest energy quarter which in moderate areas will be mostly attributed to mean tree height, is influenced by both canopy height variability and terrain slope. *e_44*, the proportion of energy in the highest elevation quarter which has significant negative effect on mean tree height, represents the portion of energy in high energy peaks which are typically ground peaks [46]. By using negative value of *e_44*, we can reduce the impact of terrain slope to some extent. w_{g4}, the fourth width of Gaussian peaks determined by Gaussian decomposition which somewhat increases with mean tree height, represents the steepening angle of the fourth reflective surface.

The model for the $>20°$ slope category replaces *startpeak* as the most useful predictor variable with a_{g4}. It can be explained that the fourth amplitude of Gaussian peaks represents the roughness of the fourth reflective surface which increases with mean tree height. *e_14* and *e_44* have significant negative effects on mean tree height. The former is related to canopy height variability and indicates the energy response of the uppermost part of trees; the latter is related to terrain slope and indicates the energy response of the "signal end" [41]. These two indices are closely related to two indices (that are, leading edge extent and trailing edge extent) that Lefsky *et al.* [19] suggest. w_{g6}, the width

of the lowest Gaussian peak is identified as a characteristic of ground surface and contributes to the model. This could be due to broadening and mix of ground and trees in high relief areas.

The results from the mean tree height model for all data show that two most important variables are *wf_extent* and *E_14*, and that the use of proportional energy metrics is useful to determine mean tree height within GLAS footprint. Meanwhile, characteristics of the fourth Gaussian curve from Gaussian decomposition (like amplitude and width) play important roles in studying the prediction for tree height.

In the past, the scientists focused on the finding of the ground peak to estimate maximum tree height. Few people estimated mean tree height, especially Lorey's height derived from GLAS data. Due to the complex terrain conditions, it is difficult to identify the precise ground elevation from Gaussian peaks. Meanwhile, please mind the obvious height differences among trees and trees locate toward the edge of the footprint. Gaussian decomposition makes determining mean tree height easy, because the number of Gaussian curves can be manipulated and the ground elevation does not need to be calculated.

V. Conclusion

In this study, we demonstrated that Lorey's height can be directly predicted from GLAS waveform information and Gaussian decomposition results under sloping terrain. The principal results obtained can be summarized as follows:

Using the extracted metrics from GLAS waveform to predict the airborne-estimated stand height, we constructed stepwise regression models to explore what waveform metrics influenced mean tree height over mountainous areas. The proportion of energy and characteristics of the Gaussian curves played important roles in studying the prediction for tree height. The models explained 87.0%, 76.7%, and 82.8% of the variation of mean tree height for the terrain slope categories of 0°–20°, $>20°$, and all data, respectively.

The results provide confidence that, although the prediction was substantially well for the situations on moderate slopes (0°–20°), the fit remained at an interesting level even for stands on slopes above 20°. But more research is still needed to further reduce the terrain effect on estimating Lorey's height, especially short stands on steep slopes.

In this paper, we present a proof of concept that GLAS data can be used to estimate Lorey's height. Similarly, the results described herein can be used to make regional, subcontinental measurements of forest biomass, and aboveground carbon. Although these results are encouraging, they should be viewed in the context of the limitations of the study. First, we considered only coniferous forest, but broadleaf forest did not be included in this study. Second, the airborne lidar point density is about 1 point per square meter, which may miss some tree height information especially to the coniferous forest because of canopy shape.

References

[1] M. Nilsson, "Estimation of tree heights and stand volume using an airborne lidar system," *Remote Sens. Environ.*, vol. 56, pp. 1–7, Jan. 1996.

[2] M. A. Lefsky, W. B. Cohen, G. G. Parker, and D. J. Harding, "Lidar remote sensing for ecosystem studies: Lidar, an emerging remote sensing technology that directly measures the three-dimensional distribution of plant canopies, can accurately estimate vegetation structural attributes and should be of particular interest to forest, landscape, and global ecologists," *BioScience*, vol. 52, pp. 19–30, Jan. 2002.

[3] P. Hyde, R. Dubayah, B. Peterson, J. Blair, M. Hofton, C. Hunsaker *et al.*, "Mapping forest structure for wildlife habitat analysis using waveform lidar: Validation of montane ecosystems," *Remote Sens. Environ.*, vol. 96, pp. 427–437, Jun. 2005.

[4] S. C. Popescu, "Estimating biomass of individual pine trees using airborne lidar," *Biomass Bioenergy*, vol. 31, pp. 646–655, Sep. 2007.

[5] S. C. Popescu, R. H. Wynne, and R. F. Nelson, "Measuring individual tree crown diameter with lidar and assessing its influence on estimating forest volume and biomass," *Can. J. Remote Sens.*, vol. 29, no. 5, pp. 564–577, May 2003.

[6] S. C. Popescu and K. Zhao, "A voxel-based lidar method for estimating crown base height for deciduous and pine trees," *Remote Sens. Environ.*, vol. 112, pp. 767–781, Mar. 2008.

[7] H. D. V. Boehm, L. Veraldo, and S. H. Suwido, "Multi-temporal airborne LiDAR-survey and field measurements of tropical peat swamp forest to monitor changes," *IEEE J. Sel. Topics Appl. Earth Observ. Remote Sens.*, vol. 6, no. 3, pp. 1524–1530, Jun. 2013.

[8] V. Thomas, P. Treitz, J. McCaughey, and I. Morrison, "Mapping stand-level forest biophysical variables for a mixedwood boreal forest using lidar: An examination of scanning density," *Can. J. Forest Res.*, vol. 36, no. 1, pp. 34–47, Jan. 2006.

[9] K. Eiji and A. Yoshio, "Estimating mean height and stand volume in broad leaved forest stands using LiDAR," *J. Forest Plan. Jpn.*, vol. 13, pp. 239–243, Feb. 2008.

[10] A. O. Onojeghuo and G. A. Blackburn, "Characterising reedbeds using LiDAR data: Potential and limitations," *IEEE J. Sel. Topics Appl. Earth Observ. Remote Sens.*, vol. 6, no. 2, pp. 935–941, Apr. 2013.

[11] M. A. Lefsky, "A global forest canopy height map from the moderate resolution imaging spectroradiometer and the geoscience laser altimeter system," *Geophys. Res. Lett.*, vol. 37, p. L1540101-05, Aug. 2010.

[12] M. Simard, N. Pinto, J. B. Fisher, and A. Baccini, "Mapping forest canopy height globally with spaceborne lidar," *J. Geophys. Res. Biogeo. (2005–2012)*, vol. 116, p. G04021, Dec. 2011.

[13] B. Schutz, H. Zwally, C. Shuman, D. Hancock, and J. DiMarzio, "Overview of the ICESat mission," *Geophys. Res. Lett.*, vol. 32, p. L21S01, Nov. 2005.

[14] Y. Shi, S. Choi, X. Ni, S. Ganguly, G. Zhang, H. Duong *et al.*, "Allometric scaling and resource limitations model of tree heights: Part 1. Model optimization and testing over Continental USA," *Remote Sens.*, vol. 5, pp. 284–306, Jan. 2013.

[15] M. Chopping, M. North, J. Chen, C. B. Schaaf, J. B. Blair, J. V. Martonchik *et al.*, "Forest canopy cover and height from MISR in topographically complex southwestern US landscapes assessed with high quality reference data," *IEEE J. Sel. Topics Appl. Earth Observ. Remote Sens.*, vol. 5, no. 1, pp. 44–58, Feb. 2012.

[16] M. A. Lefsky, W. Cohen, S. Acker, G. G. Parker, T. Spies, and D. Harding, "Lidar remote sensing of the canopy structure and biophysical properties of Douglas-fir western hemlock forests," *Remote Sens. Environ.*, vol. 70, pp. 339–361, Dec. 1999.

[17] V. Duong, R. Lindenbergh, N. Pfeifer, and G. Vosselman, "Single and two epoch analysis of ICESat full waveform data over forested areas," *Int. J. Remote Sens.*, vol. 29, pp. 1453–1473, Mar. 2008.

[18] A. L. Neuenschwander, T. J. Urban, R. Gutierrez, and B. E. Schutz, "Characterization of ICESat/GLAS waveforms over terrestrial ecosystems: Implications for vegetation mapping," *J. Geophys. Res. Biogeo. (2005–2012)*, vol. 113, p. G02S0301-18, Jun. 2008.

[19] M. A. Lefsky, M. Keller, Y. Pang, P. B. De Camargo, and M. O. Hunter, "Revised method for forest canopy height estimation from geoscience laser altimeter system waveforms," *J. Appl. Remote Sens.*, vol. 1, pp. 013537-013537–18, Sep. 2007.

[20] S. C. Popescu, K. Zhao, A. Neuenschwander, and C. Lin, "Satellite lidar vs. small footprint airborne lidar: Comparing the accuracy of aboveground biomass estimates and forest structure metrics at footprint level," *Remote Sens. Environ.*, vol. 115, pp. 2786–2797, Nov. 2011.

[21] G. Sun, K. Ranson, D. Kimes, J. Blair, and K. Kovacs, "Forest vertical structure from GLAS: An evaluation using LVIS and SRTM data," *Remote Sens. Environ.*, vol. 112, pp. 107–117, Jan. 2008.

[22] Q. Chen, "Retrieving vegetation height of forests and woodlands over mountainous areas in the Pacific Coast region using satellite laser altimetry," *Remote Sens. Environ.*, vol. 114, pp. 1610–1627, Jul. 2010.

[23] Q. Chen, "Assessment of terrain elevation derived from satellite laser altimetry over mountainous forest areas using airborne lidar data," *ISPRS J. Photogramm.*, vol. 65, pp. 111–122, Oct. 2010.

[24] Y. Xing, A. de Gier, J. Zhang, and L. Wang, "An improved method for estimating forest canopy height using ICESat-GLAS full waveform data over sloping terrain: A case study in Changbai mountains, China," *Int. J. Appl. Earth Observ.*, vol. 12, pp. 385–392, Oct. 2010.
[25] S. Lee, W. Ni-Meister, W. Yang, and Q. Chen, "Physically based vertical vegetation structure retrieval from ICESat data: Validation using LVIS in white mountain national forest, New Hampshire, USA," *Remote Sens. Environ.*, vol. 115, pp. 2776–2785, Nov. 2011.
[26] K. Ioki, J. Imanishi, T. Sasaki, Y. Morimoto, and K. Kitada, "Estimating stand volume in broad-leaved forest using discrete-return LiDAR: Plot-based approach," *Landsc. Ecol. Eng.*, vol. 6, pp. 29–36, Jan. 2010.
[27] E. Næsset, "Airborne laser scanning as a method in operational forest inventory: Status of accuracy assessments accomplished in Scandinavia," *Scand. J. Forest Res.*, vol. 22, pp. 433–442, Nov. 2007.
[28] S. Hall, I. Burke, D. Box, M. Kaufmann, and J. Stoker, "Estimating stand structure using discrete-return lidar: An example from low density, fire prone ponderosa pine forests," *Forest Ecol. Manage.*, vol. 208, pp. 189–209, Apr. 2005.
[29] J. A. van Aardt, R. H. Wynne, and R. G. Oderwald, "Forest volume and biomass estimation using small-footprint lidar-distributional parameters on a per-segment basis," *Forest Sci.*, vol. 52, no. 6, pp. 636–649, Dec. 2006.
[30] F. Loetsch, F. Zohrer, and K. E. Haller, *Forest Inventory.* Munchen, Germany: BLV Verlagsgesellschaft, 1973.
[31] M. Nicola, C. Rosa, and L. Rosa. (2011, Apr.). *Laser Scanning: Theory and Applications* [Online]. Available: http://www.intechopen.com/books/laser-scanning-theory-and-applications.
[32] P. Axelsson. (2000). DEM generation from laser scanner data using adaptive TIN models, *presented at XIX ISPRS Congress, Commission IV* [Online]. Available: http://www.isprs.org/proceedings/XXXIII/congress/part4/111_XXXIII-part4.pdf.
[33] A. T. Hudak, N. L. Crookston, J. S. Evans, D. E. Hall, and M. J. Falkowski, "Nearest neighbor imputation of species-level, plot-scale forest structure attributes from LiDAR data," *Remote Sens. Environ.*, vol. 112, pp. 2232–2245, May 2008.
[34] A. T. Hudak, N. L. Crookston, J. S. Evans, M. J. Falkowski, A. M. Smith, P. E. Gessler *et al.*, "Regression modeling and mapping of coniferous forest basal area and tree density from discrete-return lidar and multispectral satellite data," *Can. J. Remote Sens.*, vol. 32, no. 2, pp. 126–138, Jan. 2006.
[35] J. E. Means, S. A. Acker, B. J. Fitt, M. Renslow, L. Emerson, and C. J. Hendrix, "Predicting forest stand characteristics with airborne scanning lidar," *Photogramm. Eng. Remote Sens.*, vol. 66, no. 11, pp. 1367–1372, Nov. 2000.
[36] J. S. Evans, A. T. Hudak, R. Faux, and A. Smith, "Discrete return LiDAR in natural resources: Recommendations for project planning, data processing, and deliverables," *Remote Sens.*, vol. 1, pp. 776–794, Oct. 2009.
[37] A. C. Brenner, H. J. Zwally, C. R. Bentley, B. Csathó, D. Harding, and M. Hofton *et al.* (2003, Sep.). *Derivation of Range and Range Distributions From Laser Pulse Waveform Analysis for Surface Elevations, Roughness, Slope, and Vegetation Heights*, Greenbelt, MD: Goddard Space Flight Center [Online]. Available: http://www.csr.utexas.edu/glas/pdf/Atbd_20031224.pdf.
[38] M. E. Miller, M. Lefsky, and Y. Pang, "Optimization of geoscience laser altimeter system waveform metrics to support vegetation measurements," *Remote Sens. Environ.*, vol. 115, pp. 298–305, Feb. 2011.
[39] M. A. Hofton, J. B. Minster, and J. B. Blair, "Decomposition of laser altimeter waveforms," *IEEE Trans. Geosci. Remote Sens.*, vol. 38, no. 4, pp. 1989–1996, Jul. 2000.
[40] C. B. Markwardt, "Non-linear least squares fitting in IDL with MPFIT," arXiv:0902.2850, Feb. 2009.
[41] L. I. Duncanson, K. O. Niemann, and M. A. Wulder, "Estimating forest canopy height and terrain relief from GLAS waveform metrics," *Remote Sens. Environ.*, vol. 114, pp. 138–154, Jan. 2010.
[42] R. Nelson, K. Ranson, G. Sun, D. Kimes, V. Kharuk, and P. Montesano, "Estimating Siberian timber volume using MODIS and ICESat/GLAS," *Remote Sens. Environ.*, vol. 113, pp. 691–701, Mar. 2009.
[43] R. M. O'brien, "A caution regarding rules of thumb for variance inflation factors," *Qual. Quant.*, vol. 41, pp. 673–690, Oct. 2007.
[44] M. Stone, "Cross-validatory choice and assessment of statistical predictions," *J. Roy. Stat. Soc. B (Methodol.)*, vol. 36, no. 2, pp. 111–147, Dec. 1974.
[45] S. Geisser, "The predictive sample reuse method with applications," *J. Am. Stat. Assoc.*, vol. 70, no. 350, pp. 320–328, Jun. 1975.
[46] D. J. Harding and C. C. Carabajal, "ICESat waveform measurements of within footprint topographic relief and vegetation vertical structure," *Geophys. Res. Lett.*, vol. 32, p. L21S1001-04, Nov. 2005.

Zhou Fang was born in Jiangxi, China, in 1986. He received the B.S. degree in surveying and mapping from Jilin University, Jilin, China, in 2008, and the M.S. degree in photogrammetry and remote sensing from Wuhan University, Hubei, China, in 2010. He is currently pursuing the Ph.D. degree in cartology and GIS at the Institute of Remote Sensing and Digital Earth (RADI), Chinese Academy of Sciences (CAS), Beijing, China.

His research interests are airborne and spaceborne lidar data processing, forest structural parameters extraction, and remote sensing inversion modeling.

Chunxiang Cao was born in Inner-Mongolia, China. She received the M.S. degree in forest remote sensing from Kyoto Prefectural University, Kyoto, Japan, in 1996, and the Ph.D. degree in environmental planning and remote sensing from Hiroshima University, Hiroshima, Japan, in 2000.

Since 2000, she has been a Researcher with RADI, CAS. Currently, she is a Director of the Department of Environmental Health Remote Sensing at IRSDE. Her research interests include diagnosis of environmental health by remote sensing, mainly including forest remote sensing, quantitative remote sensing inversion of ecological environmental parameters, and public health research using spatial information technology.